



ORIGINAL ARTICLE

The synthesis of the P/N-type $\text{NdCoO}_3/\text{g-C}_3\text{N}_4$ nano-heterojunction as a high-performance photocatalyst for the enhanced photocatalytic degradation of pollutants under visible-light irradiation



Salimeh Kianipour^a, Fatemeh Sadat Razavi^a, Morteza Hajizadeh-Oghaz^b, Waleed K. Abdulsahib^c, Makarim A. Mahdi^d, Layth S. Jasim^d, Masoud Salavati-Niasari^{a,*}

^a Institute of Nanoscience and Nanotechnology, University of Kashan, Kashan, P.O. Box 87317-51167, Iran

^b Department of Materials Science and Engineering, Esfarayen University of Technology, Esfarayen, North Khorasan, Iran

^c Department of Pharmacology and Toxicology, College of Pharmacy, Al-Farahidi University, Baghdad, Iraq

^d Department of Chemistry, College of Education, University of Al-Qadisiyah, Diwaniya, Iraq

Received 4 January 2022; accepted 13 March 2022

Available online 16 March 2022

KEYWORDS

Carbon nitride;
Eriochrome black T;
Neodymium cobaltite;
Photocatalysis;
Sol-gel autocombustion;
Visible-light irradiation

Abstract The treatment of industrial and domestic colored effluents and the use of photocatalysts have today attracted much attention among researchers. With the varied photocatalytic materials, the ones with narrow bandgap are thus of greater significance thanks to their acceptable performance in optical fields. The other obvious property of such materials is their lower costs because a large part of sunlight is in the visible region. In this work, the bare perovskite-type neodymium cobaltite and neodymium cobaltite/graphite carbon nitride (p/n-type $\text{NdCoO}_3/\text{g-C}_3\text{N}_4$) was synthesized using sol-gel auto combustion. Different reductants were also employed during this fabrication for morphological engineering, such as glucose (carbohydrate), L-valine (amino acid), and citric acid. As well, X-ray diffraction analysis (XRD), Fourier transform infrared spectroscopy (FTIR), and energy-dispersive X-ray spectroscopy (EDS) were utilized to prove the purity of the specimens, and then transmission electron microscopy (TEM) and field-emission scanning electron microscopy (FE-SEM) were applied to explore their morphology. The various properties of the product, such as the optical, magnetic, porosity, and surface features, were correspondingly checked by diffuse reflectance spectroscopy (DRS), photoluminescence (PL) spectroscopy, vibrating-sample

* Corresponding author.

E-mail address: salavati@kashanu.ac.ir (M. Salavati-Niasari).

Peer review under responsibility of King Saud University.



magnetometry (VSM), and Brunauer-Emmett-Teller (BET) surface area analysis, respectively. Citric acid was thus selected as an optimal fuel because of the formation of finer particles and morphology. In addition, the NdCoO₃ nanoparticles (NPs) were exploited as a catalyst for the degradation of anionic dyes (viz. erythrosine [Red No. 3], methyl orange [MO], and eriochrome black T [EBT]) and cationic ones (i.e., rhodamine B [RhB], acid red 14 [ACR14], and acid yellow 23 [AY23]) under visible-light irradiation. The study findings accordingly revealed that the heterostructures emerged at the interfaces between the p-type NdCoO₃ and n-type g-C₃N₄, leading to the EBT decolorization, reached 95.8% after 120 min, and were higher than the photodegradation of the pristine NdCoO₃ and g-C₃N₄.

© 2022 The Author(s). Published by Elsevier B.V. on behalf of King Saud University. This is an open access article under the CC BY-NC-ND license (<http://creativecommons.org/licenses/by-nc-nd/4.0/>).

1. Introduction

Over recent decades, technological and scientific advancements along with researchers' efforts have significantly contributed to the treatment of industrial and domestic effluents and the improvement of drinking water (Zhang et al., 2019; Omrani and Nezamzadeh-Ejehieh, 2020; Zhang et al., 2020a,b; Zhang et al., 2021). Among the effective methods to resolve this dilemma is photodegradation, using ultraviolet (UV) or visible-light irradiation and nano-semiconductors as catalysts. This method is simple, green, and at approximately a low cost, so it has attracted much attention in the industry and among researchers (Ghanbari et al., 2016; Zhang et al., 2020a,b; Zhang et al., 2021). Nano-semiconductors can be thus assumed as helpful catalysts for photoactivity because of reducing particle size and high surface area (Di Mauro et al., 2015; Wu et al., 2015; Heidari-Asil et al., 2020; Zhou et al., 2021).

However, nanocatalysts have thus far solved many problems corresponding to photocatalytic ones due to their distinctive properties. Researchers are still constantly trying to find innovations; for example, the high rate of recombination of the photo-induced electron and the hole is one of the relevant problems. In addition to doping and loading metals, one solution is to create a heterojunction made by two semiconductors. This strategy, employing semiconductor conduction and valance bands, can accordingly assist in the better separation of electron-hole pairs (He et al., 2020; Xu et al., 2020; Ranjeh et al., 2021; Zhou et al., 2021). On the other hand, researchers have focused more on visible-light-driven semiconductors, perovskite-type oxides, and graphitic carbon nitride (g-C₃N₄), rather than UV ones. Both g-C₃N₄ and perovskite materials are a good choice in photocatalysis owing to their structural stability and being affordable and active under visible-light irradiation (particularly, narrow bandgap) (Luo et al., 2019; Monga and Basu 2019; Chen et al., 2020, Faisal et al., 2020, Rokesh et al., 2020).

The polymeric semiconductor, g-C₃N₄, also possesses two-dimensional (2D) aromatic sheets in the form of a tri-s-triazine structure with the highest stability compared with its other allotropes (Shi et al., 2014; Gaddam et al., 2020). Nonetheless, the low photoactivity of g-C₃N₄ stems from the low separation of the electron-hole pair in this semiconductor. Consequently, it is essential to enhance the photo performance of the n-type g-C₃N₄ couples with another semiconductor to produce p/n-type heterojunction, which is helpful to separate electrons and holes (Christoforidis et al., 2016a,b; Li et al., 2019; Ghane and Sadrezaad, 2020; Ismael, 2020; Melchionna and Fornasiero, 2020; Yang et al., 2021; Xu et al., 2022). Of note, g-C₃N₄ behaves as an n-type semiconductor because of the presence of electron donors in its structure (i.e., -NH/NH₂ groups) (Fu et al., 2018). The reported bandgap for g-C₃N₄ is around 2.7 eV in the visible region. (Azami et al., 2020; Liao et al., 2020). Moreover, many perovskite materials (e.g., ABO₃) in single, metal-doped, or composite forms, such as strontium stannate (SrSnO₃) (Teixeira et al., 2019), strontium titanate/cobalt ferrite (SrTiO₃/CoFe₂O₄), strontium cations doped in

potassium tantalate (KTaO₃) (Sudrajat et al., 2019), graphite carbon nitride/silver/lanthanum ferrite (g-C₃N₄/Ag/LaFeO₃) (Gao et al., 2019), β-Fe₂O₃/g-C₃N₄ nanocomposite (Christoforidis et al., 2016a, b), TiO₂/carbon nitride heterojunctions (Christoforidis et al., 2019) and palladium/cerium-manganese oxidase 3 (Pd-CeMnO₃) (Yi et al., 2018) have been synthesized and applied as photocatalysts.

Until recently, there has been much interest in lanthanum cobaltite (LaCoO₃), as a member of the multicopper oxidase 3 (MCoO₃) perovskite family, synthesized via different methods, such as sol-gel auto combustion and coprecipitation (CPT) (Maulana and Nandiyanto, 2019). Furthermore, this special perovskite has been manufactured in various forms, e.g., silver phosphate/lanthanum cobaltite (Ag₃PO₄/LaCoO₃) nanocomposite (Guo et al., 2017), iron (Fe) and bismuth (Bi) doping on LaCoO₃ (Ajmal et al., 2019), La_{1-x}Sr_xCoO₃/Ag₃PO₄ (Chen et al., 2021), and LaCoO₃/g-C₃N₄ (Luo et al., 2018). Lanthanide perovskites are also effective photocatalysts in the presence of visible illumination because of their high stability and environmentally friendly features; however, it is better to improve their photocatalytic performance by adding other materials to separate more electrons and holes. Therefore, neodymium cobaltite (NdCoO₃) as an n-type lanthanide perovskite is appropriate for photocatalytic issues that have recently received less attention (Ali et al., 2011; Ling et al., 2016; Guo et al., 2019; Nakhostin Panahi et al., 2020).

This work, as the first attempt in this line, explores the role of synthesized NdCoO₃ nanoparticles (NPs) using sol-gel auto combustion, as a catalyst for the decolorization of erythrosine [Red No. 3], methyl orange (MO), and eriochrome black T [EB] as anionic dyes and rhodamine B [RhB], acid red 14 [ACR14], and acid yellow 23 [AY23] as cationic ones. Finally, a comparison was made between the photoperformance efficiency of g-C₃N₄, NdCoO₃, and NdCoO₃/g-C₃N₄ heterojunction for the EBT degradation. To the best of the authors' knowledge, there was no study on photocatalytic dye degradation using NdCoO₃/g-C₃N₄, PN-type heterojunction.

2. Experimental study

2.1. Materials

For the synthesis of the NdCoO₃/g-C₃N₄ nanocomposite, all chemicals were used from the Merck & Co. (USA) in a pure form, including melamine (C₃H₆N₆), cobalt (II) nitrate (Co(NO₃)₂·6H₂O), neodymium nitrate (Nd(NO₃)₃·6H₂O), glucose (C₆H₁₂O₆), citric acid (C₆H₈O₇), and L-valine (C₅H₁₁NO₂). In this work, the dyes utilized as water pollution factors, i.e., Red No. 3 (C₂₀H₆I₄Na₂O₅), RhB (C₂₈H₃₁ClN₂O₃), EBT (C₂₀H₁₂N₃O₇SNa), ACR14 (C₂₀H₁₂N₂Na₂O₇S₂), MO (C₁₄H₁₄N₃NaO₃S), and AY23 (C₁₆H₉N₄Na₃O₉S₂) were also acquired from Sigma-Aldrich Corp. (USA).

2.2. Fabrication of NdCoO₃ NPs

As indicated in Fig. 1, the NdCoO₃ NPs were created by various fuels, such as L-valine, citric acid, and glucose employed in this study. First, neodymium salt (0.075 g) and fuel (0.134 g glucose, 0.143 g citric acid, and 0.08 g L-valine) were separately dissolved in distilled water with a molar ratio of 1:4, respectively. Next, under a magnetic stirrer at 60 °C, the prepared fuel of the solution, as a reductant and morphological engineering agent, was added to the solution containing neodymium nitrate. After 30 min according to the molar ratio selected, 1:1 for Nd:Co, an aqueous solution of cobalt (II) nitrate (0.05 g) was added into the solution placed on the magnetic stirrer by heating the solution at 120 °C for 60 min, the solvent was evaporated, and hence the viscose gel was formed. Afterward, the gel obtained was placed in the oven at 70 °C for one day. Finally, the dried violet product was calcinated at 600 °C for 2 h. In this method, citric acid and other fuels were further used as reducing and capping agents. The schematic diagram of the formation of the NdCoO₃ nanostructures by different fuels is shown in Fig. 1.

2.3. Fabrication of g-C₃N₄

To form g-C₃N₄, melamine powder was utilized thoroughly by direct heating. For this purpose, first, white melamine powder was placed into a crucible, and then, it was calcinated in the atmosphere at 550 °C for 4 h. Finally, the yellow g-C₃N₄ powder was formed.

2.4. Fabrication of NdCoO₃/g-C₃N₄ nanocomposite

In this part, the NdCoO₃/g-C₃N₄ nanocomposite was prepared in an ex-situ route. First, 0.1 g NdCoO₃ was obtained by citric acid as an optimum fuel, as a morphologically optimal sample, with 0.3 g g-C₃N₄, and then sonicated in 30 ml ethanol for 40 min. Next, the suspension was stirred at room temperature for a day. Then, the suspension was heated at 50 °C under stir-

ring to evaporate the solvent. Then after, the cement-shape sediment was dried at 70 °C for 24 h, and subsequently ground in a mortar. Finally, the NdCoO₃/g-C₃N₄ sample with 25- wt % was synthesized. The preparation conditions of the products are listed below (Table 1), and the schematic diagram of the NdCoO₃/g-C₃N₄ nanocomposite preparation is illustrated in Fig. 2.

2.5. Photocatalytic test

First, 0.05 g of NdCoO₃ was weighed and added to 50 ml of 5-ppm dye-containing solution. Next, the sample placed on the stirrer magnetic was 15 cm outdistance from the light source. Then, the sample was stirred without light for half an hour before irradiating until it reached balancing adsorption-desorption. Subsequently, with the onset of light illumination, a certain amount of the sample was gathered every 20 min and then centrifuged. Finally, the solution adsorption was studied by UV-Vis spectrometry at a specific wavelength. The percentage of the destruction of the dyes was calculated as:

$$\text{Degradation rate} = \frac{(C_0 - C)}{C_0} \times 100 \quad (1)$$

wherein C_0 refers to the primary concentration, and C stands for the concentration at the reaction time t .

2.6. Characterization

To explore the crystallite size, purity, and phase composition of the synthesized samples, a diffractometer of Philips Co. (Netherlands, i.e., the X-ray diffraction analysis [XRD]) was used with copper K- α (Cu K α) radiation. The crystallite size was thus computed using the full width at half maximum (FWHM) data from this technique and the Scherrer equation as follows:

$$d = \frac{0.9\lambda}{\beta \cos\theta} \quad (2)$$

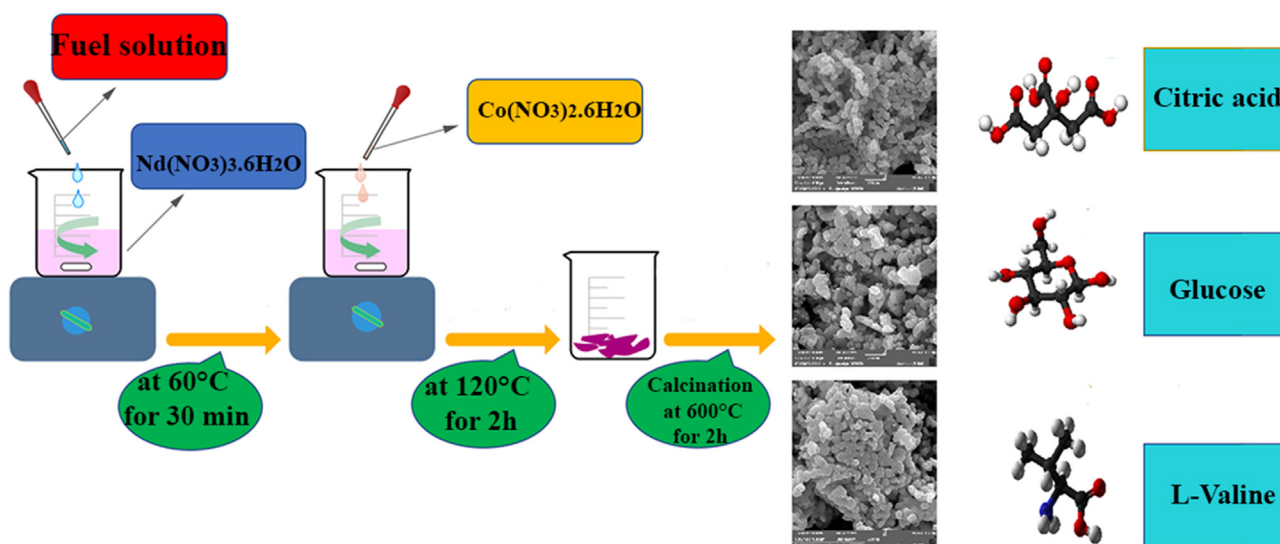
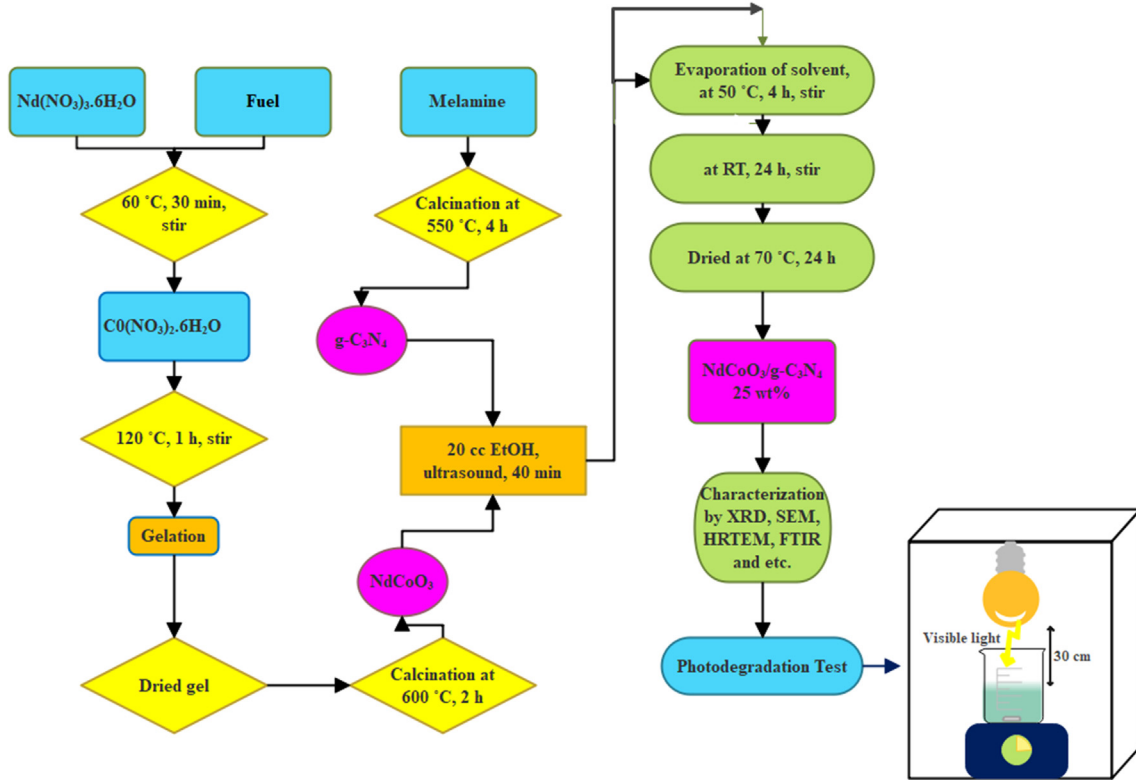


Fig. 1 Schematic of the formation of NdCoO₃ nanostructures by different fuels.

Table 1 The preparation conditions for the products.

Sample No.	Fuel	g-C ₃ N ₄ :NdCoO ₃	Calcination temperature (°C)	Products
1	Citric acid	0: 1	600	NdCoO ₃
2	Glucose	0: 1	600	NdCoO ₃
3	L-valine	0: 1	600	NdCoO ₃
4	Citric acid	1: 3	600	NdCoO ₃ /g-C ₃ N ₄
5	–	1: 0	550	g-C ₃ N ₄

**Fig. 2** Schematic diagram of the preparation of NdCoO₃/g-C₃N₄ nanocomposite.

in which, d represents the crystallite size (nm), λ shows 1.54 Å corresponding to the Cu K α radiation, β refers to the FWHM data, Θ indicates the Bragg angle, and 0.9 is the constant-related dimensionless shape factor.

Fourier transform infrared spectroscopy (FTIR; Shimadzu, FTIR-4300 spectrophotometer, Japan) on potassium bromide (KBr) pellets was also used to examine the chemical bonds of the prepared samples. Employing field emission-scanning electron microscopy (FE-SEM, LMU TESCAN BRNO-Mira3, Czech Republic) and transmission electron microscopy (TEM, Philips Co. EM208, Netherlands, with an accelerating voltage of 100 kV), the particle size and surface morphologies of the photocatalysts were studied, respectively. The specific surface area was further investigated by the Brunauer-Emmett-Teller (BET) surface area analysis (BELsorp mini II, Japan) for the thorough adsorption and desorption of nitrogen gas at its boiling point. The optical property of the nanostructures was then examined by exploiting a spectrophotometer (UV-vis, Shimadzu, UV-2550, Japan) and photoluminescence

spectroscopy (PL, optical luminescence, Perkin Elmer Co., LS-55, USA). Utilizing the below equation and drawing the Tauc plot, the bandgap resulting from the absorption data was then acquired:

$$(\alpha h\nu)^{\frac{1}{n}} = A(h\nu - E_g) \quad (3)$$

wherein, α is the observed semiconductor absorption, A shows the constant, $h\nu$ refers to the photon energy, E_g indicates the optical bandgap (eV), and n is 2 for the direct or 1/2 for the indirect bandgap semiconductor. Furthermore, the bandgap from the PL emission data was estimated (Eq. (4)), as follows:

$$E_g = \frac{1240}{\lambda} \quad (4)$$

The magnetic feature was also explored with a vibrating-sample magnetometer (VSM, Meghnatis Kavir Kashan Co, Iran). Moreover, the synthesis of the NdCoO₃/C₃N₄ nanocomposite was carried out by a sonicator (Bandelin Sonopuls HD 3200, Germany).

3. Results and discussion

3.1. XRD

The XRD patterns related to the fabricated samples, depicted in Fig. 3, confirm the successful formation of all specimens with high crystallinity. The g-C₃N₄ hexagonal phase also has a faint peak, and a strong peak at $2\theta = 13.0^\circ$, corresponding to (100) plane and $2\theta = 27.6^\circ$ ascribed to (002) plane (Moakhar et al., 2020; Munusamy et al., 2021), respectively. The feeble peak is due to the in-plane structural packing motif of the tri-s-triazine units ($d = 0.680$ nm). The stronger one is also attributed to the interlayer stacking of the aromatic rings ($d = 0.325$ nm) (Zhao et al., 2014; Papailias et al., 2020). As for NdCoO₃ with an orthorhombic structure, six characteristic peaks are obviously at $2\theta = 23.6^\circ, 33.6^\circ, 41.5^\circ, 48.2^\circ, 60.0^\circ$ and 70.5° , ascribed to (101), (121), (220), (202), (123) and (242) crystal planes, sequentially (Ateia et al., 2019). Thus, NdCoO₃ is fabricated in a pure form with the help of all three fuels. Fig. 3d reveals the major diffraction peaks of NdCoO₃ and g-C₃N₄, indicating a good interaction between them. Interestingly, the NdCoO₃/g-C₃N₄ nanocomposite has a high crystallinity, too. Furthermore, the NdCoO₃/g-C₃N₄ grain size measured by the Scherer equation, $D = 0.9\lambda/\beta\cos\theta$, is obtained at 23 nm.

3.2. FTIR

As shown in Fig. 4, the peaks of the bare NdCoO₃, corresponding to the vibrating and stretching of Nd-Co-O and Co-O, are 577 and 473 cm^{-1} , respectively, similar to DyCoO₃ and LaCoO₃ (Xiong et al., 1997; Michel et al., 2019; Phadtare et al., 2019). As for the g-C₃N₄, the peak located at 806 cm^{-1} is ascribed to the triazine (viz. the breathing vibration) (Wang et al., 2020). The wide range in the $3000\text{--}3500$ cm^{-1} is further associated with the N-H and NH₂ groups (namely, the stretching and bending vibration) (Zi et al., 2021). The bending and

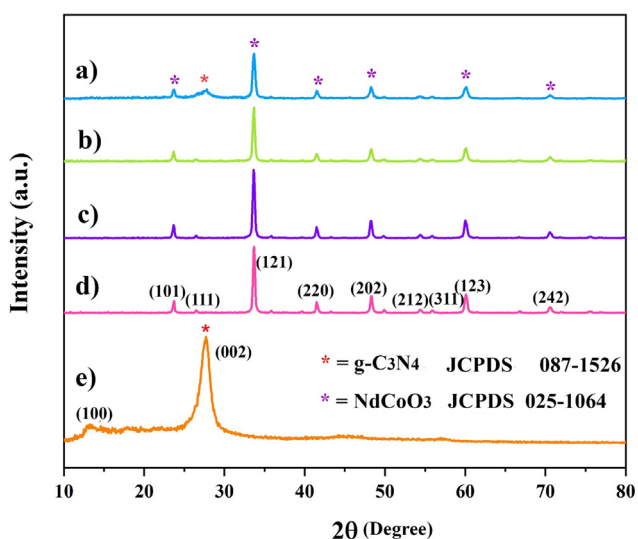


Fig. 3 XRD pattern of (a) NdCoO₃/g-C₃N₄, (b) NdCoO₃ (valine), (c) NdCoO₃ (glucose), (d) NdCoO₃ (citric acid), (e) g-C₃N₄ powders.

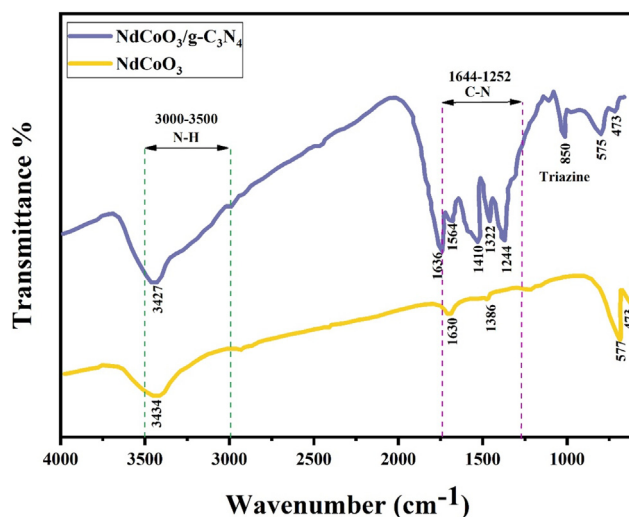


Fig. 4 FT-IR spectrum of pure NdCoO₃ nanostructure (sample No. 1), and NdCoO₃/g-C₃N₄ nanocomposite.

stretching vibration modes of water sitting on the NP surfaces are also observed at 1630 and 3430 cm^{-1} , respectively.

3.3. TEM, FE-SEM, and EDS

Fig. 5 depicts the micro-images of NdCoO₃ prepared through the reaction between metal nitrates as oxidizing and fuels as reducing agents. The fuels used for this purpose also have different chelating effects because of their functional (viz. hydroxyl and carboxyl) groups. Hence, the morphology and particle size of the synthesized nanostructures are shaped by the chemical structure of the fuel. The glucose structure also has five hydroxyl groups (OH⁻), whereas that of L-valine and citric acid has one and three carboxyl acid groups, respectively. Moreover, the hydroxyl group has a weaker electron-donating group than the carboxyl one. So, L-valine has a less chelating ability than glucose and citric acid (Yahya et al., 2018). For this reason, the synthesized samples with L-valine and glucose aggregated more than those with citric acid. Similarly, the average particle size calculated by the ImageJ software was around 20.7 nm (L-valine), 19.4 nm (glucose), and 17.4 nm (citric acid) (Fig. 5). Likewise, the sample produced by citric acid has been selected as an optimum because of better morphology and smaller average particle size.

Fig. 6 illustrates the FE-SEM and TEM images of the prepared NdCoO₃/g-C₃N₄ nanocomposite in the presence of optimum fuel (citric acid) in different scales. Both NdCoO₃ and layered structure g-C₃N₄ are distinguishable in Fig. 6f. The resulting photos and the particle size distribution histogram reveal the increase in the size of the particles. The particle size received from TEM is usually smaller than that in FE-SEM due to the lack of gold coating of the surfaces in TEM and not SEM. Nevertheless, owing to the agglomerate phenomenon in the nanocomposite, this subject was reversed in this research. Moreover, the crystallite size calculated from the XRD pattern is 23 nm and smaller than the FE-SEM and TEM outcomes, which shows the particles are composed of crystallites.

The EDS spectrum of the NdCoO₃ NPs fabricated by diverse reductants, the NdCoO₃/g-C₃N₄ nanocomposite, and

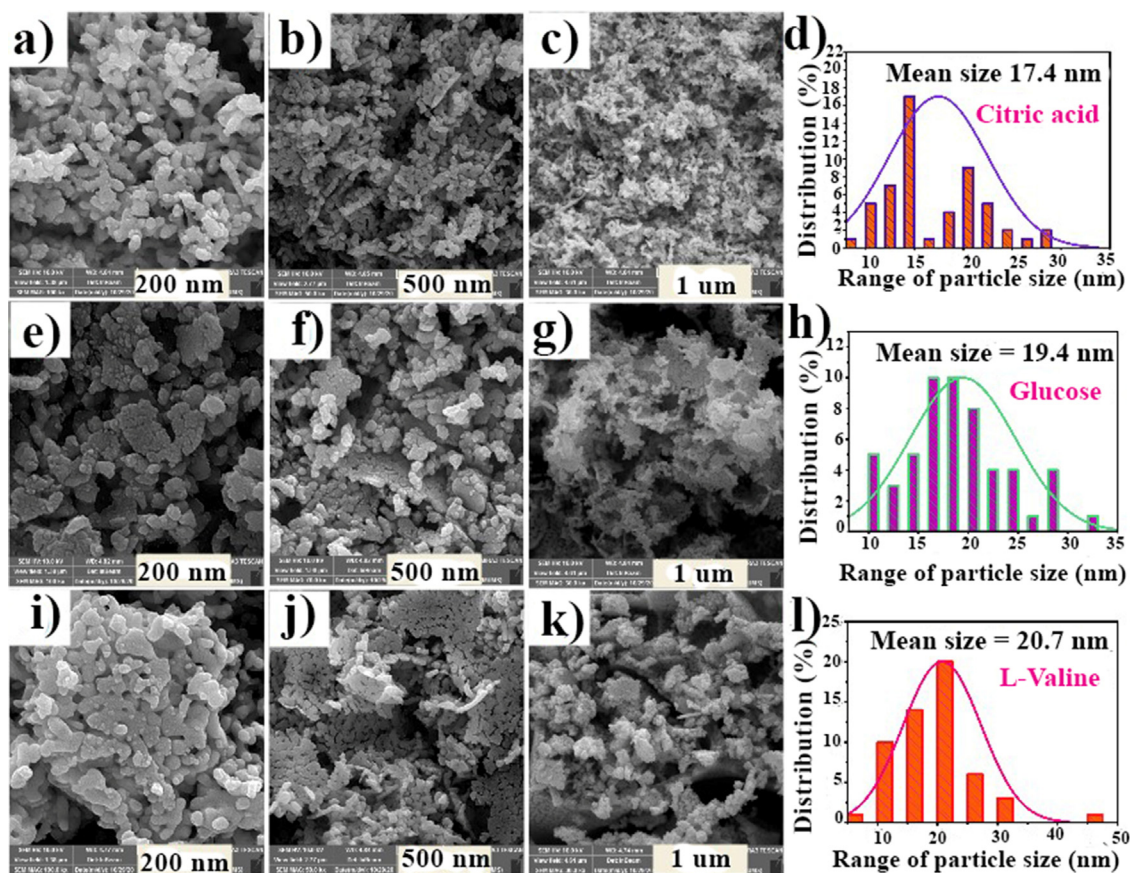


Fig. 5 FE-SEM images of the fabricated NdCoO_3 nanoparticles by various reductant and associated average particle size histogram: (a-d) citric acid, (e-h) glucose, (i-l) valine in different scales.

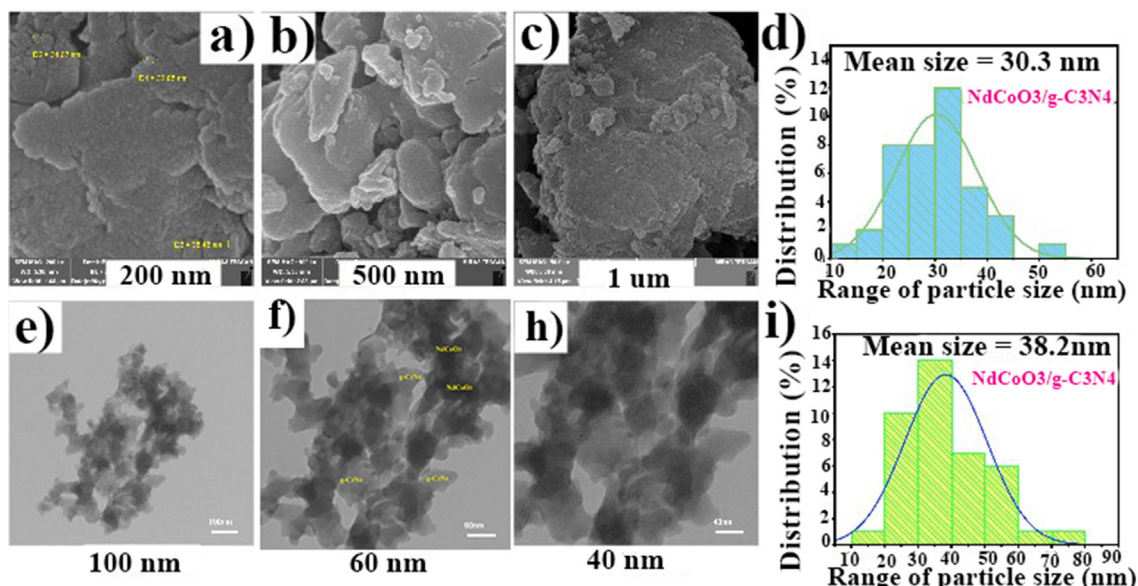


Fig. 6 FE-SEM and TEM images of prepared $\text{NdCoO}_3/\text{g-C}_3\text{N}_4$ nanocomposite corresponding average particle size histogram.

the percentage of all elements are further displayed in Fig. 7(a-d). The EDS results also prove the purity of the products. This pattern demonstrates the existence of N, Co, O, Nd, and C elements in the fabricated nanocomposite.

3.4. VSM

The magnetic measurement of the $\text{NdCoO}_3/\text{g-C}_3\text{N}_4$ nanocomposite was performed at the ambient temperature using a

VSM. As shown in Fig. 7e, the linear H/M plot depicts the NdCoO₃/g-C₃N₄ nanocomposite as a paramagnetic compound. Of note, the paramagnetic behavior is due to the presence of NdCoO₃ in nanocomposites. The coercivity (H_c), remnant magnetization (M_r), saturation magnetization (M_s), and squareness (M_r/M_s) also have approximated around 189 Oe, 7.93 × 10⁻³ emu/g, 0.352 emu/g, and 0.022, sequentially.

3.5. BET surface area analysis

Fig. 7f demonstrates the BET surface area analysis of the NdCoO₃/g-C₃N₄ nanocomposite. The adsorption-desorption isotherm curve is similar to the type-III and H3-type hysteresis in conformity with the International Union of Pure and Applied Chemistry (IUPAC) classification. The specific surface area of the nanocomposite was approximately 9.94 m²/g, and the total pore volume measured was around 2.284 cm³/g. On the other hand, the average pore diameter was 27 and

22 nm, according to the BET and Barrett-Joyner-Halenda (BJH) analysis data plots. Thereby, both results of the particle size perfectly matched the FE-SEM and TEM consequences.

3.6. UV-Vis absorbance spectral analysis

Using UV-Vis diffuse reflectance spectroscopy (DRS) helped measure the optical features of g-C₃N₄ and NdCoO₃ NPs. As shown in Fig. 8(a-c), the suitable absorptions of both are observed in the range of about 200–450 nm, and the absorption of NdCoO₃ is a little more than carbon nitride. On the other hand, the bandgap is obtained, using Eq. (3), and then the graph between (αhν)^{1/2} vs. the hν, Tauc plot. Likewise, the bandgaps are 2.73 and 2.79 eV for g-C₃N₄ and NdCoO₃, indicating them as sufficient catalysts to photodegrade colored effluents under visible-light irradiation, especially when they are together as a composite.

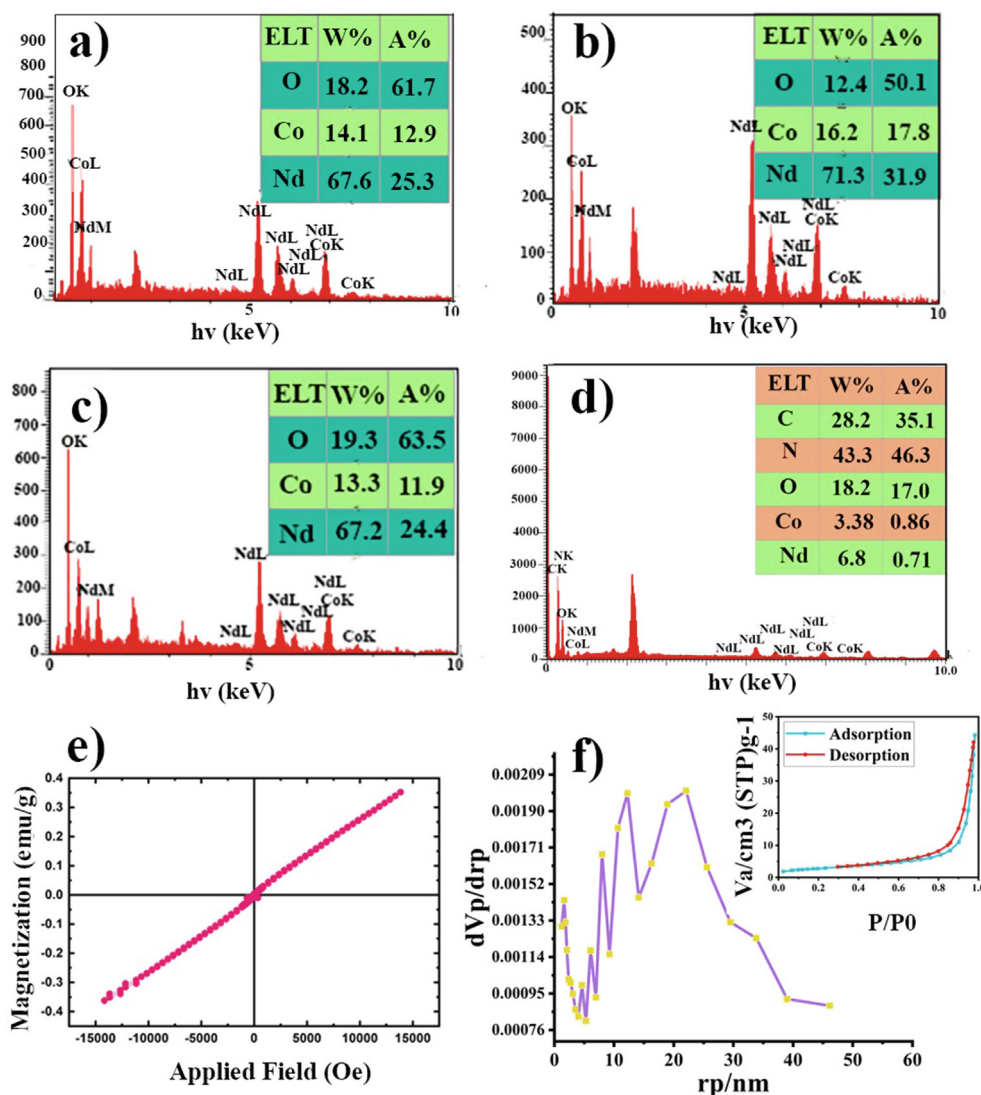


Fig. 7 EDS spectrum related to the synthesized NdCoO₃ by (a) citric acid, (b) valine, (c) glucose, (d) NdCoO₃/g-C₃N₄, (e) VSM curve and (f) BJH and N₂ absorption-desorption (inset) of the NdCoO₃ (sample No.1).

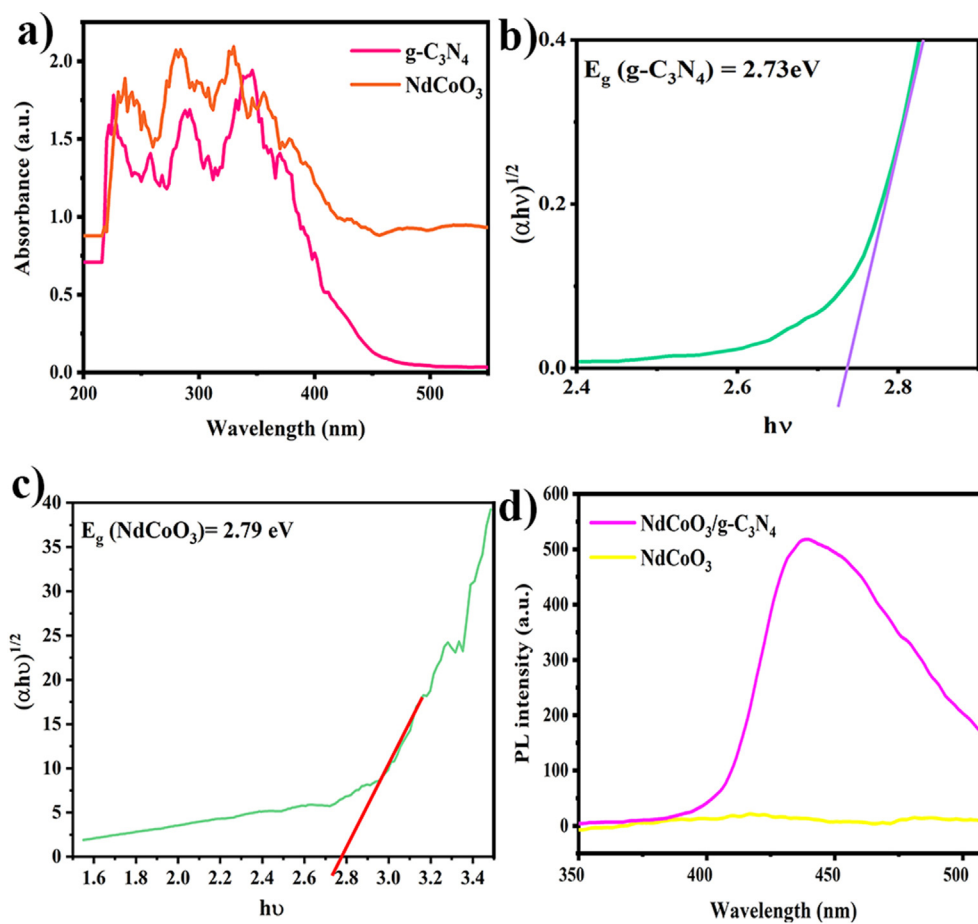


Fig. 8 (a) UV-Vis DRS spectrum of $g\text{-C}_3\text{N}_4$ and NdCoO_3 (sample No.1); the plot of bandgap energies for (b) $g\text{-C}_3\text{N}_4$ (sample No.5), and (c) NdCoO_3 (sample No.1); (d) PL spectra of $\text{NdCoO}_3/g\text{-C}_3\text{N}_4$ (sample No.4).

3.7. PL spectroscopy

The photoluminescence spectra of the bare NdCoO_3 and $g\text{-C}_3\text{N}_4/\text{NdCoO}_3$ are demonstrated in Fig. 8d. The PL of a single NdCoO_3 does not show any PL signals. As reported by (Chen et al., 2014), the single $g\text{-C}_3\text{N}_4$, on account of the recombination of the photogenerated electron-hole pairs, can have a clear fluorescence emission peak at 455 nm. Thus, the observed fluorescence signal around 439 nm is associated with carbon nitride in the composite in the PL of the $g\text{-C}_3\text{N}_4/\text{NdCoO}_3$ nanocomposite, establishing a good interaction between NdCoO_3 and $g\text{-C}_3\text{N}_4$, which leads to a blue-shift in the PL spectra of the $\text{NdCoO}_3/g\text{-C}_3\text{N}_4$ nanocomposite compared with the bare $g\text{-C}_3\text{N}_4$, at 455 nm (Jin et al., 2019a,b). Finally, the bandgap of the $\text{NdCoO}_3/g\text{-C}_3\text{N}_4$ nanocomposite is estimated at 2.82 eV by the $1240/\lambda$ equation.

3.8. Photocatalytic activity

The catalytic performance of the NdCoO_3 NPs was surveyed for the decolorization of different dyes as effluents under visible-light irradiation (400 W). Afterward, the effect of diverse parameters such as the catalyst dosage, pH, scavenger, and the role of $g\text{-C}_3\text{N}_4$ added to the NdCoO_3 , was studied on the optimal dye in terms of higher photodegradation. A dark

experiment in the absence of irradiation was performed for 30 min to test whether the absorption of the EBT caused the decolorization of EBT by the nanoparticles. EBT concentration did not decrease obviously, indicating that decolorizing of EBT is mostly due to photodegradation rather than adsorption. Summary performed photocatalytic result is tabled (Table 2).

3.8.1. Impact of dye

Fig. 9 (a and b) illustrates the photocatalytic performance of NdCoO_3 for 5 ppm of anionic organic dyes (via. MO, Red No. 3, and EBT) and the cationic organic ones (namely, RhB, ACR14, and AY23) as pollutants in industrial wastewater. The most decolorization of the anionic dyes is associated with EBT (58.2%), and this value is 26.8% and 35.5% for MO and Red No. 3, respectively. As shown in the photocatalyst plot, the highest degradation of the cationic dyes is related to ACR14 (48.8%). Sequentially, the percentage of the decolorization of RhB and AY23, the other cationic dyes, is 25.7% and 38.0%. Hence, it seems that NdCoO_3 is a better catalyst for the EBT anionic dyes.

3.8.2. Effect of catalyst loading

Fig. 9c demonstrates a comparison between the 0.025 g, 0.05 g, and 0.075 g of the nanocatalyst on the photocatalytic

Table 2 Summary table of performed photocatalytic result.

Photocatalyst	Dye	Catalyst loading (g)	Initial pH	Scavenger	Degradation%
NdCoO ₃	RhB (cationic)	0.05 g	7	–	25.7%
NdCoO ₃	ACR14 (cationic)	0.05 g	7	–	48.8%
NdCoO ₃	AY23 (cationic)	0.05 g	7	–	38.0%
NdCoO ₃	MO (anionic)	0.05 g	7	–	26.8%
NdCoO ₃	Erythrosine (anionic)	0.05 g	7	–	35.5%
NdCoO ₃	EBT (anionic)	0.05 g	7	–	52.8%
NdCoO ₃	EBT (anionic)	0.025	7	–	47.2%
NdCoO ₃	EBT (anionic)	0.075	7	–	70.2%
NdCoO ₃	EBT (anionic)	0.075	3	–	89.9%
NdCoO ₃	EBT (anionic)	0.075	3	EDTA	74.4%
NdCoO ₃	EBT (anionic)	0.075	3	Benzoquinone	90.6%
NdCoO ₃	EBT (anionic)	0.075	3	Benzoic acid	55.5%
g-C ₃ N ₄	EBT (anionic)	0.075	3	–	81.8%
NdCoO ₃ /g-C ₃ N ₄	EBT (anionic)	0.075	3	–	95.8%

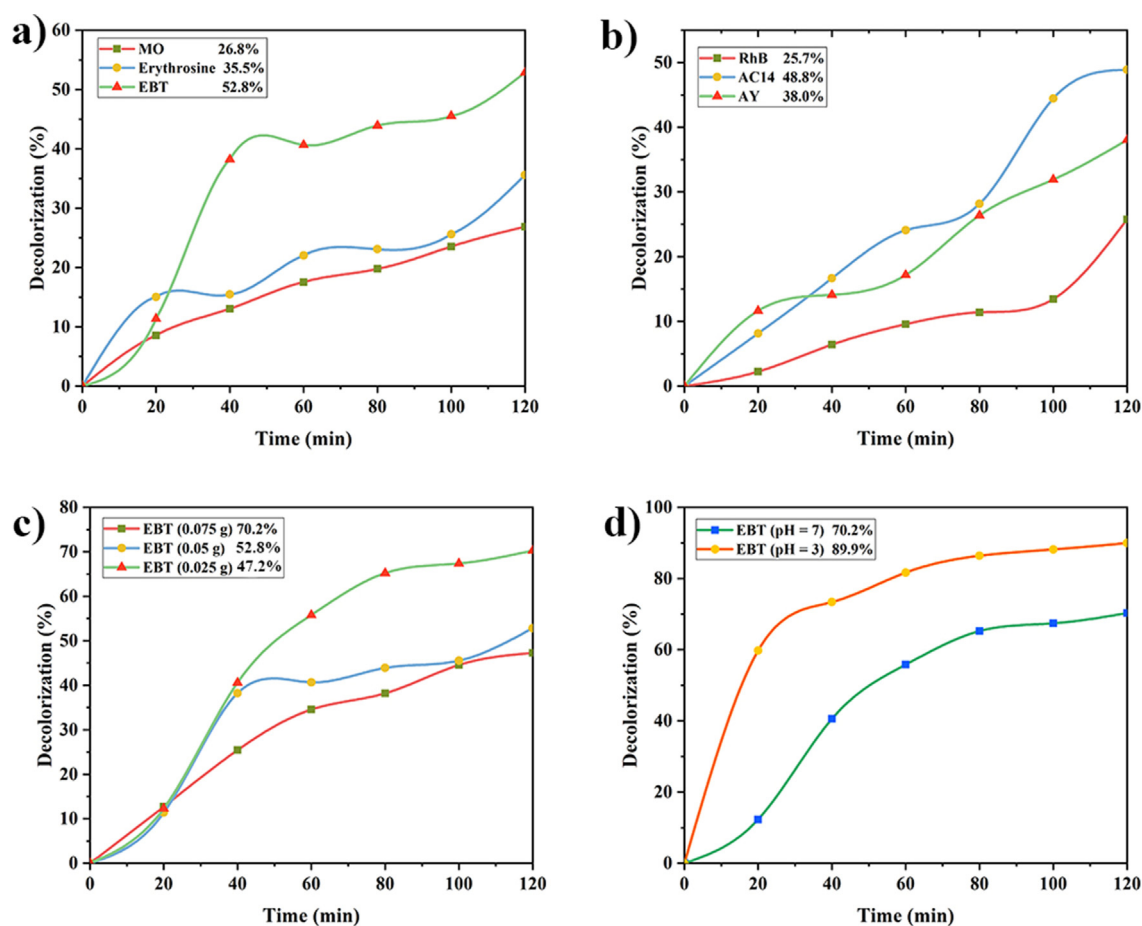


Fig. 9 A comparison between the photocatalytic performances NdCoO₃ (0.05 g, sample No.1) nanoparticle (pH = 7) in the presence of (a) anionic dyes and (b) cationic dyes (5 ppm). A comparison between the photocatalytic performances of NdCoO₃ (sample No.1), for degradation of EBT (5 ppm) under visible-light irradiation in the different (a) catalyst dosage (pH = 7) and in the different (b) pH environments (0.07 g of NdCoO₃, sample No.1).

behavior. With the growing amount of NdCoO₃, the catalytic performance increases. The leading cause of this incremental routine is aligned with the rise in the available surface area. As shown in the degradation plot, when the 0.025 g of the

catalyst is used, the percentage of the decolorization of EBT is obtained as 47.2%. Once the 0.05 g and 0.07 g of the sample are utilized, the degradation efficiency is by 52.8% and 70.2%, respectively. Consequently, 0.075 g of

NdCoO₃ as a photocatalyst for the EBT contaminant was the ideal dosage.

3.8.3. Effect of Initial pH

In this section, the EBT decolorization was inspected in an acidic and natural environment. A comparison of the two results revealed the photocatalyst performance in an acidic medium (pH = 3), which was better than natural environment (pH = 7). This behavior was owned to the presence of H⁺ caused by the acidic environment, which could lead to more electrostatic attraction and, consequently, more relationship between the active surface of the catalyst and the pollutant. As denoted in Fig. 9d, 70.2% of EBT in the natural environment and 89.9% of EBT in the acidic environment is degraded by the NdCoO₃ NPs within 120 min.

3.8.4. Scavenger-quenching impact

This step aimed to recognize the effective active species (i.e., h⁺, ·OH, and ·O₂⁻) in the EBT decolorization. Therefore, three scavengers, including benzoic acid, EDTA, and benzoquinone,

were exploited for trapping ·OH, h⁺, and ·O₂⁻, respectively (Zhang et al., 2019). According to Fig. 10a, the influence of benzoquinone on the photocatalytic process is similar to the no-scavenger sample, and the EBT destruction is at a maximum (90%). Hence, the superoxide radical is not used in the photocatalytic process. On the other hand, the addition of the hole (EDTA) and the hydroxyl radical (BA) agents reduced the percentage of decolorization to 74.4% and 55.5%, respectively. The descending decolorization rates also demonstrated that h⁺ played a minor role and ·OH was the prominent active radical in the EBT degradation.

3.8.5. Synergetic performance

The photocatalytic behavior of NdCoO₃, g-C₃N₄, and NdCoO₃/g-C₃N₄ was assessed under visible-light irradiation for 120 min. As exhibited in Fig. 10c, the single phases show a lower decolorization percentage than nanocomposite. Moreover, this value is 89.9% for NdCoO₃ and 81.8% for g-C₃N₄. Because of adding g-C₃N₄ to NdCoO₃, the electron-hole separation is enhanced. Thereby, these parts together as a composite ameliorate the catalytic activity. The final percentage of the

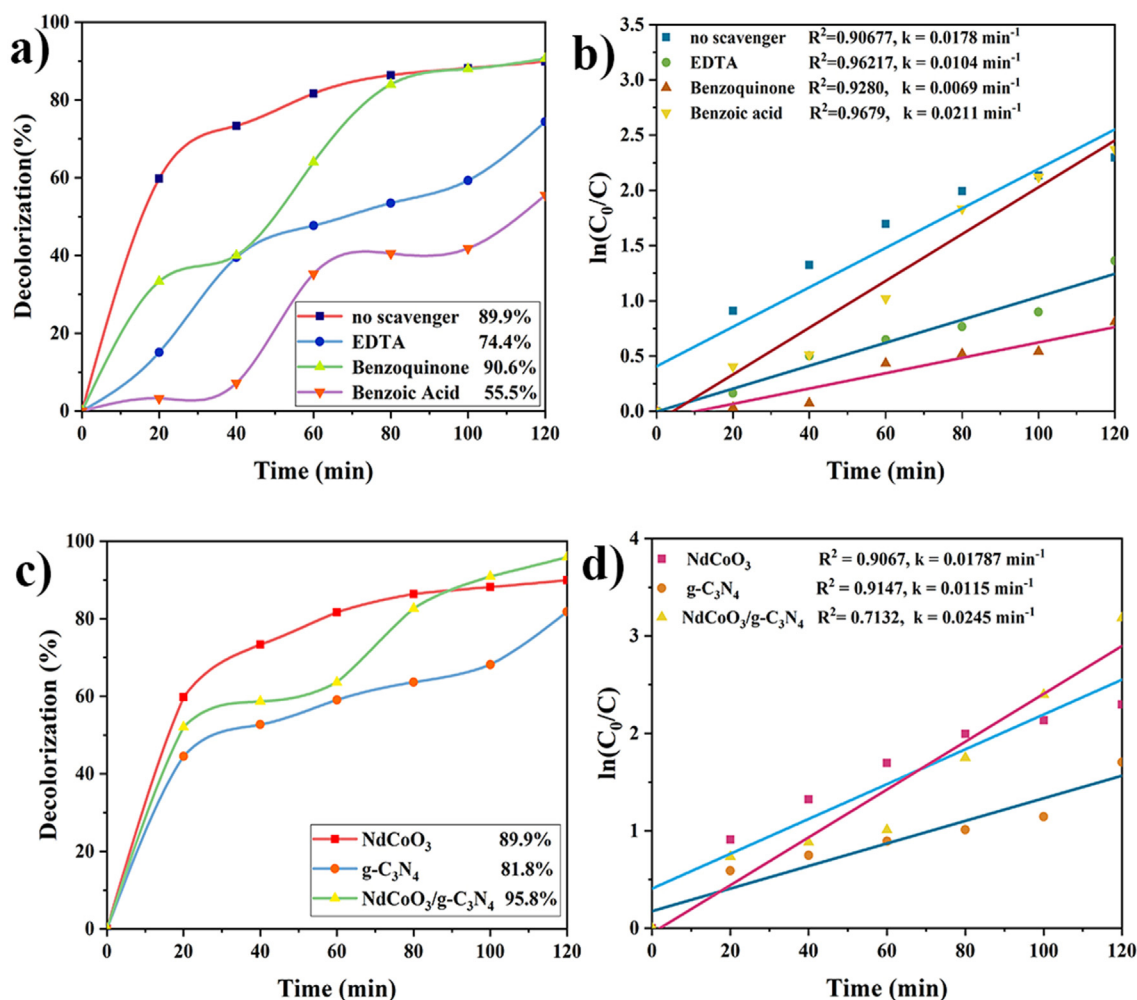


Fig. 10 The photocatalytic performances of (a) NdCoO₃ nanoparticles (0.05 g, sample No.1) for degradation of EBT (5 ppm, pH = 3) in the presence of different scavengers and (c) NdCoO₃ (sample No.1) compared with g-C₃N₄ and NdCoO₃/g-C₃N₄ (0.05 g of catalyst, 5 ppm, pH = 3). (b and d) Plots of ln(C₀/C) vs. time.

EBT decolorization by the NdCoO₃/g-C₃N₄ nanocomposite also reached 95.8%.

3.8.6. Photodegradation pathway

Creating a p/n-type heterojunction between NdCoO₃ (p-type, E_f located near the valence band, VB) and g-C₃N₄ (n-type, E_f located near conduction band, CB) creates an electric field between their contact interfaces. The CB and VB potential of NdCoO₃ (p-type) and g-C₃N₄ (n-type) are thus indispensable to ascertain a possible mechanism between them. Accordingly, the E_{CB} (viz. the conduction band edge) and E_{VB} (namely, the valence band edge) for the semiconductors can be computed utilizing the following empirical formula:

$$E_{CB} = \chi - E_e - 0.5E_g \quad (4)$$

$$E_{VB} = E_{VB} + E_g \quad (5)$$

wherein, χ exhibits the electronegativity of the semiconductor, E_e displays the energy of free electrons on the hydrogen scale (4.5 eV vs. NHE), and E_g indicates the semiconductor band-

gap. The electronegativity and the bandgap values (with reference to the DRS results) for g-C₃N₄ are 4.73 eV (Liu, 2015; Porcu et al., 2020) and 2.73 eV, respectively. Additionally, the χ and the bandgap of the pure NdCoO₃ NPs are obtained at 5.59 eV and 2.79 eV. Consequently, using the χ and E_e values, the E_{CB} and the E_{VB} of NdCoO₃ are nearly determined to be -0.238 eV and 2.55 eV, and the E_{CB} and the E_{VB} of g-C₃N₄ are calculated to be around -1.13 eV and 1.59 eV, respectively. Fig. 11 shows the schematic diagram of the intended mechanism related to NdCoO₃, g-C₃N₄, and the NdCoO₃/g-C₃N₄ nanocomposite. The O₂ adsorbed on the nanocomposite surface was thus reduced by placing the electrons than E_{O_2/O_2^-} (Eq. 2). The photogenerated electrons of the CB of NdCoO₃ accordingly fail to reduce the O₂ to superoxide radical ($E_{CB} = -0.238$ eV, $E_{O_2} = -0.35$ eV (Armstrong et al., 2015)). The hydroxyl radicals are generated by the photo-induced hole in the VB of NdCoO₃ due to $E_{VB} = 2.55$ eV and $E_{OH^-/OH\cdot} = 1.90$ eV (Armstrong et al., 2015) (Eq. 3), but the hole in the VB of g-C₃N₄ does not generate \cdot OH because of its more

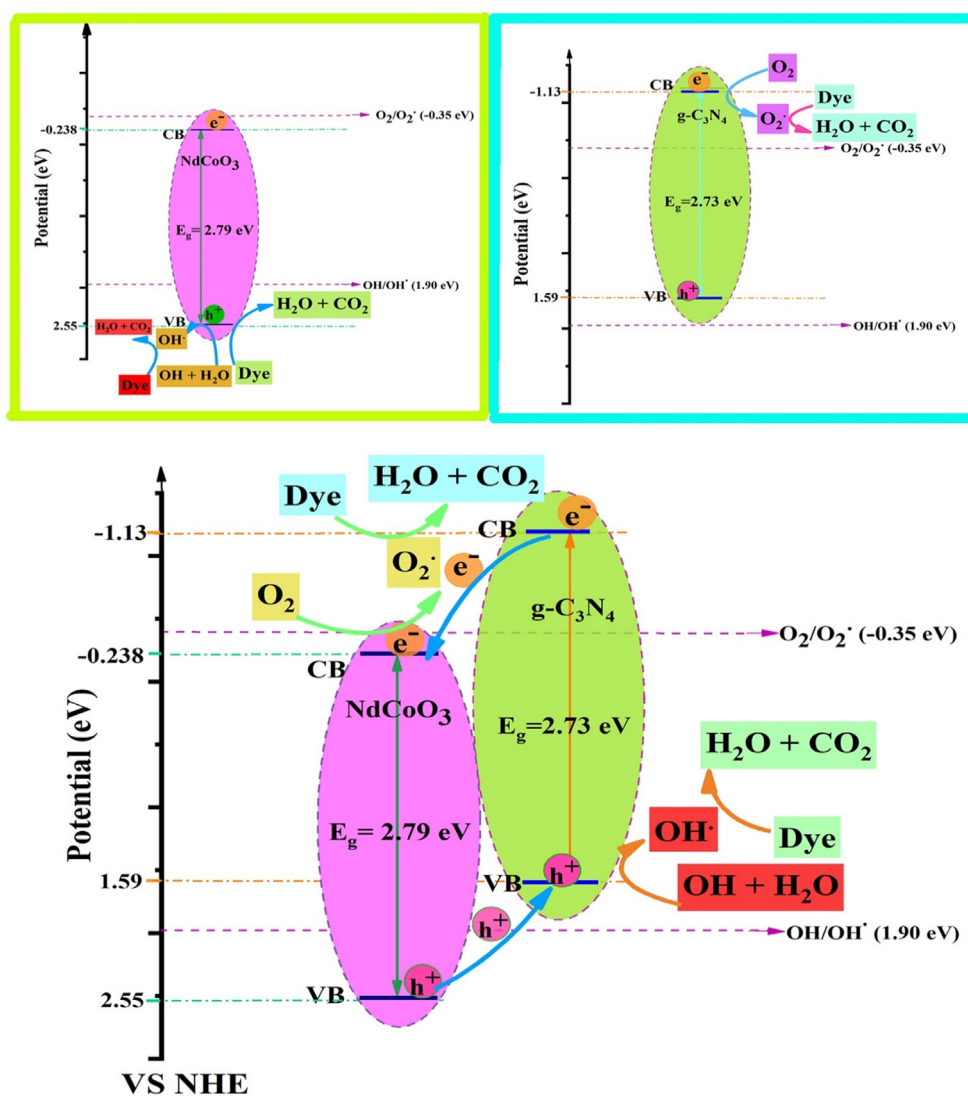
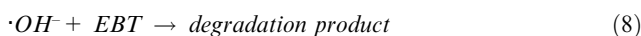
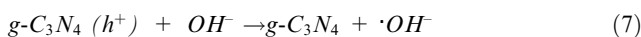
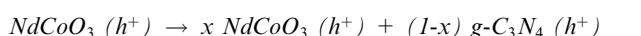
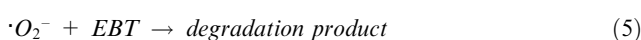
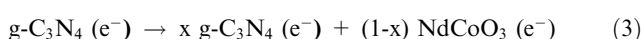
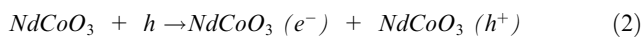
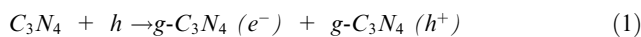


Fig. 11 Photocatalytic mechanism scheme of bare NdCoO₃ (sample No.1), g-C₃N₄ (sample No.5), and NdCoO₃/g-C₃N₄ (sample No.4), heterojunction nanocomposites under visible light irradiation.

positive potential than the hydroxyl potential ($E_{VB} = 1.59$ eV, $E_{OH^-/OH} = 1.90$). Therefore, $NdCoO_3/g-C_3N_4$ has formed the heterojunction structure, which helps all reactions co-occur in a composite material, as displayed in Fig. 11. Consequently, the triggered electrons migrate from the CB of $g-C_3N_4$ to that of the $NdCoO_3$. Likewise, the photogenerated holes in the VB of $NdCoO_3$ relocate to the VB of $g-C_3N_4$. Finally, the generated h^+ , OH^\cdot , and O_2 (as the active species) in $NdCoO_3/g-C_3N_4$ are employed for the EBT decolorization (Eqs. 5, 6, 7, 8). Thus, $NdCoO_3$ and $g-C_3N_4$ formed the heterojunction structure, which improved decolorization.



Moreover, the EBT photodegradation mechanism by the $NdCoO_3/g-C_3N_4$ nanocomposite is shown in Fig. 12. The photocatalytic properties of nanocomposites based on $g-C_3N_4$ for environmental pollution are reviewed in Table 3. The catalytic activity of all nanocomposites is affected by the precursors and fabrication methods, even though they all have $g-C_3N_4$ as the main component. Compared to singular materials, coupled nanostructures have higher photocatalytic efficiency. As a result of heterojunctions being formed in hybridized materials, there is a cooperative effect to be accomplished.

3.8.7. Kinetic study

The integral method was utilized to ascertain the order of the photocatalytic reaction. According to some surveys, the dye degradation process follows the first-order kinetics model as per:

$$\ln(C_0/C) = kt \quad (8)$$

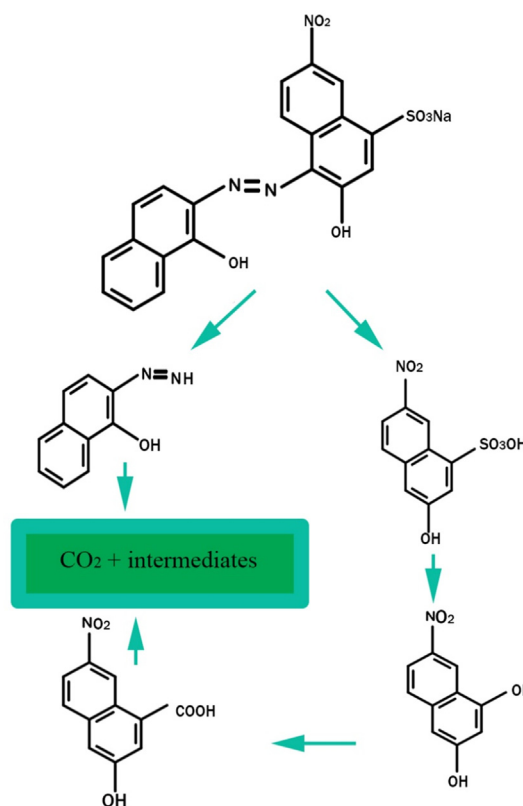


Fig. 12 Intermediate photoproducts formed and plausible pathway for the EBT photodegradation.

Table 3 The photocatalytic activity of $g-C_3N_4$ based binary heterostructures.

Materials	Optimum C_3N_4 loading	Fabrication method	Degradation efficiency	Ref.
$NdCoO_3/g-C_3N_4$	25%	Sol-gel combustion	95.8% in 120 min/Vis EBT	This work
$LaCoO_3/g-C_3N_4$	60%	Citric acid sol-gel method-sonication	85% in 5 h/Vis phenol	(Jin et al., 2019a,b)
$LaFeO_3/g-C_3N_4$	15%	Polyacrylamide gel	97.4% in 120 min/Vis RhB	(Ye et al., 2018)
Cu doped $ZnO/g-C_3N_4$	–	Hydrothermal	100% in 90 min/Vis EBT	(Ahmad and Technology 2020)
$TiSnI_3/g-C_3N_4$	100%	Coprecipitation-sonication	84.6% in 120 min/Vis RhB	(Yousefzadeh et al., 2022)
$TiO_2/g-C_3N_4$	66.7%	Solvothermal	99.3% in 120 min/Vis RhB	(Jiang et al., 2016)
$CuI/g-C_3N_4$	100%	Coprecipitation-sonication	78.6% in 120 min/Vis MO	(Ghanbari et al., 2021)
$AgI/g-C_3N_4$	100%	Hydrothermal	94.1% in 120 min/Vis MO	(Ghanbari et al., 2021)

By plotting the $\ln(C_0/C)$ vs. degradation time (120 min), the linear plot is acquired with the constant slope (k), which is the first-order rate constant (min^{-1}) associated with photocatalytic activity. At the constant temperature and pH, the value of k indeed depends only on the photocatalytic activity. As denoted in Fig. 10 (b and d), the effect of the manifold parameters on the constant rate of the photodegradation behavior was investigated, revealing that the higher the constant rate, the more acceptable the photocatalytic performance. The constant rate of NdCoO₃, g-C₃N₄, and NdCoO₃/g-C₃N₄ was further determined by 0.0178 min^{-1} , 0.0115 min^{-1} , and 0.0245 min^{-1} , respectively. Thereby, the integration of the g-C₃N₄ phase into the NdCoO₃ NPs improved the photocatalytic process.

4. Conclusion

In this study, the pristine p/n perovskite-type NdCoO₃ and NdCoO₃/g-C₃N₄ heterojunction catalysts were fabricated through sol-gel auto combustion in the presence of citric acid, L-valine, and glucose as reductants for morphological engineering. Then, the prepared samples were characterized by XRD, FTIR, EDS, FE-SEM, TEM, BET, DRS, PL, and VSM. The products were further applied as catalysts under visible-light irradiation for 2 h. Besides, various dyes were used as effluents. The outcome denoted the acidic pH and the catalyst dosage had positive effects on the efficiency degradation. On the other hand, creating a heterostructure by the NdCoO₃/g-C₃N₄ nanocomposite with a low bandgap could lead to an ascending trend in the photocatalytic rate and it has degraded 95.8% of EBT in 120 min. Likewise, it is possible to recuperate the photocatalytic performance by changing the phase percentage in the nanocomposite composition. Though the slight agglomeration of the prepared heterostructure may decline the optical degradation process, as highlighted in the related studies and observations, it seems that the NdCoO₃/g-C₃N₄ nanocomposite can upgrade the dye degradation efficiency.

CRediT authorship contribution statement

Salimeh Kianipour: Methodology, Investigation, Software, Formal analysis. **Fatemeh Sadat Razavi:** Writing – original draft, Visualization, Formal analysis, Software. **Morteza Hajizadeh-Oghaz:** Software, Formal analysis, Conceptualization, Software. **Waleed K. Abdulsahib:** Writing – review & editing, Data curation, Investigation. **Makarim A. Mahdi:** Writing – review & editing, Data curation, Investigation. **Layth S. Jasim:** Writing – review & editing, Data curation, Funding acquisition. **Masoud Salavati-Niasari:** Formal analysis, Writing – review & editing, Writing – original draft, Conceptualization, Methodology, Supervision, Project administration, Investigation, Data curation, Validation, Resources, Visualization, Funding acquisition.

Declaration of Competing Interest

The authors declare that they have no known competing financial interests or personal relationships that could have appeared to influence the work reported in this paper.

Acknowledgments

The authors hereby extend their gratitude to the Research Council of Iran National Science Foundation (INSF,

97017837) and the University of Kashan, Kashan, Iran, for supporting this work by grant No. 159271/SK1.

References

- Ahmad, I.J.S., Technology, P., 2020. Comparative study of metal (Al, Mg, Ni, Cu and Ag) doped ZnO/g-C₃N₄ composites: efficient photocatalysts for the degradation of organic pollutants. 251, 117372.
- Ajmal, S., Bibi, I., Majid, F., et al., 2019. Effect of Fe and Bi doping on LaCoO₃ structural, magnetic, electric and catalytic properties. *J. Mater. Res. Technol.* 8, 4831–4842.
- Ali, Z., Ahmad, I., Amin, B., et al., 2011. Theoretical studies of structural and magnetic properties of cubic perovskites PrCoO₃ and NdCoO₃. 406, 3800–3804.
- Armstrong, D.A., Huie, R.E., Koppenol, W.H., et al., 2015. Standard electrode potentials involving radicals in aqueous solution: inorganic radicals (IUPAC Technical Report). 87, 1139–1150.
- Ateia, E.E., Arman, M., Morsy, M., 2019. Synthesis, characterization of NdCoO₃ perovskite and its uses as humidity sensor. *Appl. Phys. A* 125, 1–9.
- Azami, M., Jalil, A., Hitam, C., et al., 2020. Tuning of the electronic band structure of fibrous silica titania with g-C₃N₄ for efficient Z-scheme photocatalytic activity. *Appl. Surf. Sci.* 512, 145744.
- Chen, C., Zhou, J., Geng, J., et al., 2020. Perovskite LaNiO₃/TiO₂ step-scheme heterojunction with enhanced photocatalytic activity. *Appl. Surf. Sci.* 503, 144287.
- Chen, J., Chen, X., Li, N., et al., 2021. Enhanced photocatalytic activity of La_{1-x}Sr_xCoO₃/Ag₃PO₄ induced by the synergistic effect of doping and heterojunction. *International Ceramics*.
- Chen, Z., Sun, P., Fan, B., et al., 2014. In situ template-free ion-exchange process to prepare visible-light-active g-C₃N₄/NiS hybrid photocatalysts with enhanced hydrogen evolution activity. *J. Phys. Chem. C* 118, 7801–7807.
- Christoforidis, K., Melchionna, M., Montini, T., et al., 2016. Solar and visible light photocatalytic enhancement of halloysite nanotubes/g-C₃N₄ heteroarchitectures. 6, 86617–86626.
- Christoforidis, K.C., Montini, T., Bontempi, E., et al., 2016. Synthesis and photocatalytic application of visible-light active β -Fe₂O₃/g-C₃N₄ hybrid nanocomposites. 187, 171–180.
- Christoforidis, K.C., Montini, T., Fittipaldi, M., et al., 2019. Photocatalytic hydrogen production by boron modified TiO₂/carbon nitride heterojunctions. 11, 6408–6416.
- Di Mauro, A., Zimbone, M., Scuderi, M., et al., 2015. Effect of Pt nanoparticles on the photocatalytic activity of ZnO nanofibers. *Nanoscale Res. Lett.* 10, 1–7.
- Faisal, M., Jalalah, M., Harraz, F.A., et al., 2020. Au nanoparticles-doped g-C₃N₄ nanocomposites for enhanced photocatalytic performance under visible light illumination. *Ceram. Int.* 46, 22090–22101.
- Fu, J., Yu, J., Jiang, C., et al., 2018. g-C₃N₄-Based heterostructured photocatalysts. 8, 1701503.
- Gaddam, S.K., Pothu, R., Boddula, R., 2020. Graphitic carbon nitride (g-C₃N₄) reinforced polymer nanocomposite systems—A review. *Polym. Compos.* 41, 430–442.
- Gao, X., Shang, Y., Liu, L., et al., 2019. A plasmonic Z-scheme three-component photocatalyst g-C₃N₄/Ag/LaFeO₃ with enhanced visible-light photocatalytic activities. *Opt. Mater.* 88, 229–237.
- Ghanbari, D., Sharifi, S., Naraghi, A., et al., 2016. Photo-degradation of azo-dyes by applicable magnetic zeolite Y–Silver–CoFe₂O₄ nanocomposites. 27, 5315–5323.
- Ghanbari, M., Salavati-Niasari, M.J.E., Safety, E., 2021. Copper iodide decorated graphitic carbon nitride sheets with enhanced visible-light response for photocatalytic organic pollutant removal and antibacterial activities. 208, 111712.
- Ghane, N., Sadrnezhaad, S., 2020. Combustion synthesis of g-C₃N₄/Fe₂O₃ nanocomposite for superior photoelectrochemical catalytic performance. *Appl. Surf. Sci.* 534, 147563.

- Guo, J., Dai, Y.-Z., Chen, X.-J., et al., 2017. Synthesis and characterization of Ag₃PO₄/LaCoO₃ nanocomposite with superior mineralization potential for bisphenol A degradation under visible light. *J. Alloy. Compd.* 696, 226–233.
- Guo, J., Li, P., Yang, Z.J.C.C., 2019. A novel Z-scheme g-C₃N₄/LaCoO₃ heterojunction with enhanced photocatalytic activity in degradation of tetracycline hydrochloride. 122, 63–67.
- He, F., Meng, A., Cheng, B., et al., 2020. Enhanced photocatalytic H₂-production activity of WO₃/TiO₂ step-scheme heterojunction by graphene modification. *Chin. J. Catal.* 41, 9–20.
- Heidari-Asil, S.A., Zinatloo-Ajabshir, S., Amiri, O., et al., 2020. Amino acid assisted-synthesis and characterization of magnetically retrievable ZnCo₂O₄-Co₃O₄ nanostructures as high activity visible-light-driven photocatalyst. 45, 22761–22774.
- Ismael, M., 2020. A review on graphitic carbon nitride (g-C₃N₄) based nanocomposites: synthesis, categories, and their application in photocatalysis. *J. Alloy. Compd.* 156446.
- Jiang, Z., Zhu, C., Wan, W., et al., 2016. Constructing graphite-like carbon nitride modified hierarchical yolk-shell TiO₂ spheres for water pollution treatment and hydrogen production. 4, 1806–1818.
- Jin, Z., Hu, R., Wang, H., et al., 2019a. One-step impregnation method to prepare direct Z-scheme LaCoO₃/g-C₃N₄ heterojunction photocatalysts for phenol degradation under visible light. *Appl. Surf. Sci.* 491, 432–442.
- Jin, Z., Hu, R., Wang, H., et al., 2019. One-step impregnation method to prepare direct Z-scheme LaCoO₃/g-C₃N₄ heterojunction photocatalysts for phenol degradation under visible light. 491, 432–442.
- Li, R., Cai, M., Xie, Z., et al., 2019. Construction of heterostructured CuFe₂O₄/g-C₃N₄ nanocomposite as an efficient visible light photocatalyst with peroxydisulfate for the organic oxidation. *Appl. Catal. B* 244, 974–982.
- Liao, J., Cui, W., Li, J., et al., 2020. Nitrogen defect structure and NO + intermediate promoted photocatalytic NO removal on H₂ treated g-C₃N₄. *Chem. Eng. J.* 379, 122282.
- Ling, F., Anthony, O.C., Xiong, Q., et al., 2016. PdO/LaCoO₃ heterojunction photocatalysts for highly hydrogen production from formaldehyde aqueous solution under visible light. 41, 6115–6122.
- Liu, J., 2015. Origin of high photocatalytic efficiency in monolayer g-C₃N₄/CdS heterostructure: a hybrid DFT study. *J. Phys. Chem. C* 119, 28417–28423.
- Luo, J., Zhou, X., Ning, X., et al., 2018. Utilization of LaCoO₃ as an efficient co-catalyst to boost the visible light photocatalytic performance of g-C₃N₄. *Sep. Purif. Technol.* 201, 309–317.
- Luo, Y., Deng, B., Pu, Y., et al., 2019. Interfacial coupling effects in g-C₃N₄/SrTiO₃ nanocomposites with enhanced H₂ evolution under visible light irradiation. *Appl. Catal. B* 247, 1–9.
- Maulana, M.I., Nandiyanto, A.B.D., 2019. Economic Evaluation of Different Solvents in the Production of LaCoO₃ Nanoparticles Prepared by the Co-precipitation Method.
- Melchionna, M., Fornasiero, P.J.A.C., 2020. Updates on the Roadmap for Photocatalysis. 10, 5493–5501.
- Michel, C.R., Lopez-Alvarez, M.A., Martinez-Preciado, A.H., et al., 2019. Novel UV Sensing and Photocatalytic Properties of DyCoO₃. 2019.
- Moakhar, R.S., Soleimani, F., Sadrnezhaad, S.K., et al., 2020. One-pot microwave synthesis of hierarchical C-doped CuO dandelions/g-C₃N₄ nanocomposite with enhanced photostability for photoelectrochemical water splitting. *Appl. Surf. Sci.* 530, 147271.
- Monga, D., Basu, S., 2019. Enhanced photocatalytic degradation of industrial dye by g-C₃N₄/TiO₂ nanocomposite: Role of shape of TiO₂. *Adv. Powder Technol.* 30, 1089–1098.
- Munusamy, T.D., Chin, S.Y., Khan, M.M.R., 2021. Physicochemical and electrochemical characterization of CdO/g-C₃N₄ nanocomposite for the photoreforming of petrochemical wastewater. *Mater. Today: Proc.* 42, 15–21.
- Nakhostin Panahi, P., Rasoulifard, M.H., Gholami, Z., et al., 2020. Synthesis of modified lanthanide nanoperovskites for photocatalytic removal of azo dyes under visible light irradiation. 1–17.
- Omrani, N., Nezamzadeh-Ejhi, A., 2020. BiVO₄/WO₃ nanocomposite: characterization and designing the experiments in photodegradation of sulfasalazine. *Environ. Sci. Pollut. Res.* 27, 44292–44305.
- Papailias, I., Todorova, N., Giannakopoulou, T., et al., 2020. Novel torus shaped g-C₃N₄ photocatalysts. *Appl. Catal. B* 268, 118733.
- Phadtare, D., Kondawar, S., Athawale, A., et al., 2019. Crystalline LaCoO₃ perovskite as a novel catalyst for glycerol transesterification. 475, 110496.
- Porcu, S., Castellino, M., Roppolo, I., et al., 2020. Highly efficient visible light phenyl modified carbon nitride/TiO₂ photocatalyst for environmental applications. 531, 147394.
- Ranjeh, M., Masjedi-Arani, M., Amiri, O., et al., 2021. Pechini sol-gel synthesis of Ni (II) doped LiMnBO₃/Li₂MnO₃/Li₂B₂O₄ nanophotocatalyst under UV-Vis irradiation. 46, 10324–10336.
- Rokesh, K., Sakar, M., Do, T.O., 2020. Calcium bismuthate (CaBiO₃): a potential sunlight-driven perovskite photocatalyst for the degradation of emerging pharmaceutical contaminants. *ChemPhotoChem*.
- Shi, Y., Jiang, S., Zhou, K., et al., 2014. Influence of g-C₃N₄ nanosheets on thermal stability and mechanical properties of biopolymer electrolyte nanocomposite films: a novel investigation. *ACS Appl. Mater. Interfaces* 6, 429–437.
- Sudrajat, H., Dhakal, D., Kitta, M., et al., 2019. Electron population and water splitting activity controlled by strontium cations doped in KTaO₃ Photocatalysts. *J. Phys. Chem. C* 123, 18387–18397.
- Teixeira, A.R.F.A., de Meireles Neris, A., Longo, E., et al., 2019. SrSnO₃ perovskite obtained by the modified Pechini method—Insights about its photocatalytic activity. *J. Photochem. Photobiol., A* 369, 181–188.
- Wang, R., Ye, C., Wang, H., et al., 2020. Z-Scheme LaCoO₃/g-C₃N₄ for efficient full-spectrum light-simulated solar photocatalytic hydrogen generation. 5, 30373–30382.
- Wu, J., Zhou, L., Ding, X., et al., 2015. Biological effect of ultraviolet photocatalysis on nanoscale titanium with a focus on physicochemical mechanism. *Langmuir* 31, 10037–10046.
- Xiong, G., Zhi, Z.L., Yang, X., et al., 1997. Characterization of perovskite-type LaCoO₃ nanocrystals prepared by a stearic acid sol-gel process. 16, 1064–1068.
- Xu, C., Zhou, Q., Huang, W.-Y., et al., 2022. Constructing Z-scheme β-Bi₂O₃/ZrO₂ heterojunctions with 3D mesoporous SiO₂ nanospheres for efficient antibiotic remediation via synergistic adsorption and photocatalysis. 1–14.
- Xu, L., Zeng, J., Li, Q., et al., 2020. Insight into enhanced visible-light photocatalytic activity of SWCNTs/g-C₃N₄ nanocomposites from first principles. *Appl. Surf. Sci.* 530, 147181.
- Yahya, N., Aziz, F., Jamaludin, A., et al., 2018. Effects of the citric acid addition on the morphology, surface area, and photocatalytic activity of LaFeO₃ nanoparticles prepared by glucose-based gel combustion methods. *Ind. Eng. Chem. Res.* 58, 609–617.
- Yang, L., Guo, J., Yang, T., et al., 2021. Self-assembly Cu₂O nanowire arrays on Cu mesh: A solid-state, highly-efficient, and stable photocatalyst for toluene degradation under sunlight. 402, 123741.
- Ye, Y., Yang, H., Wang, X., et al., 2018. Photocatalytic, Fenton and photo-Fenton degradation of RhB over Z-scheme g-C₃N₄/LaFeO₃ heterojunction photocatalysts. 82, 14–24.
- Yi, H., Xu, J., Tang, X., et al., 2018. Novel synthesis of Pd-CeMnO₃ perovskite based on unique ultrasonic intervention from combination of Sol-Gel and impregnation method for low temperature efficient oxidation of benzene vapour. *Ultrason. Sonochem.* 48, 418–423.
- Yousefzadeh, F., Yousif, Q.A., Ghanbari, M., et al., 2022. Fabrication of TiSnI₃/C₃N₄ nanocomposites for enhanced photodegradation of toxic contaminants below visible light and investigation of kinetic and mechanism of photocatalytic reaction. 118443.

- Zhang, D., Liang, S., Yao, S., et al., 2020. Highly efficient visible/NIR photocatalytic activity and mechanism of Yb³⁺/Er³⁺ co-doped Bi₄O₅I₂ up-conversion photocatalyst. 248, 117040.
- Zhang, D., Liu, H., Su, C., et al., 2019. Combustion synthesis of highly efficient Bi/BiOBr visible light photocatalyst with synergetic effects of oxygen vacancies and surface plasma resonance. 218, 1-7.
- Zhang, D., Liu, X., Wang, S., et al., 2021. Enhanced charges separation to improve hydrogen production efficiency by organic piezoelectric film polarization. 869, 159390.
- Zhang, D., Tang, Y., Qiu, X., et al., 2020. Use of synergistic effects of the co-catalyst, pn heterojunction, and porous structure for improvement of visible-light photocatalytic H₂ evolution in porous Ni₂O₃/MnO. 2Cd0. 8S/Cu₃P@ Cu₂S. 845, 155569.
- Zhao, H., Yu, H., Quan, X., et al., 2014. Fabrication of atomic single layer graphitic-C₃N₄ and its high performance of photocatalytic disinfection under visible light irradiation. *Appl. Catal. B* 152, 46–50.
- Zhou, Q., Huang, W., Xu, C., et al., 2021. Novel hierarchical carbon quantum dots-decorated BiOCl nanosheet/carbonized eggshell membrane composites for improved removal of organic contaminants from water via synergistic adsorption and photocatalysis. 420, 129582.
- Zi, T.-Q., Zhao, X.-R., Liu, C., et al., 2021. A facile route to prepare TiO₂/g-C₃N₄ nanocomposite photocatalysts by atomic layer deposition. *J. Alloy. Compd.* 855, 157446.